Journal of Non-Crystalline Solids 628 (2024) 122840

Contents lists available at ScienceDirect

Journal of Non-Crystalline Solids

journal homepage: www.elsevier.com/locate/jnoncrysol

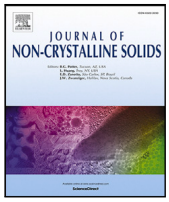

Dependence between glass transition and plasticity in amorphous aluminum oxide: A molecular dynamics study

Jiahui Zhang [a,*,1], Mikael De Meulder [a,1], Erkka J. Frankberg [b], Antti Kuronen [a]

[a] Department of Physics, University of Helsinki, Gustaf Hällströmin katu 2, 00014, Helsinki, Finland
[b] Materials Science and Environmental Engineering Unit, Tampere University, Korkeakoulunkatu 6, Tampere, 33720, Finland

ARTICLE INFO

Keywords:
Molecular dynamics simulations
Amorphous oxides
Plastic deformation

ABSTRACT

Aluminum oxide (Al_2O_3) is known to form amorphous structures that exhibit a unique plastic deforming ability at room temperature. However, alumina is considered a poor glass former, and it has been unclear whether alumina undergoes a glass transition during solidification from melt, and what effects such a transition would have on the plastic deform ability of the material. Here, we show using molecular dynamics simulations that a melt-quenched alumina indeed exhibits a glass transition, and that the glass transition greatly affects the observed material ductility. The glass transition temperature is found to positively correlate with the used cooling rate and we observe that maximum stress correlates with varying quench cooling rates in tensile test simulations, indicating that profound structural differences are formed during the glass transition. Significantly, we show that inducing plastic deformation allows erasing the structural memory of the material, and at 50% strain, all samples quenched at different rates shift again to exhibit similar flow stress. Characterizing methods that include medium-range structural information show a better ability to capture the structural differences formed during the glass transition. Our analysis results indicate that lower glass transition temperature imposes deeper potential wells of atoms and, therefore, a 'colder' structure. The mechanical work input plays a similar role as input thermal energy to the structure. A 'colder' structure needs more mechanical energy to get activated, thus showing a higher maximum stress. At a steady state flow, all samples show similar flow stress, indicating a similar structure.

1. Introduction

Amorphous materials are generally acknowledged as having short-range order but lacking long-range order compared to crystalline materials [1]. Amorphous materials are generally brittle due to their high resistance to shear flow and low resistance to crack propagation [2,3]. Instead of local deformation, they tend to fail in a catastrophic, brittle fashion, limiting their further usage. However, Frankberg et al. showed earlier that amorphous Al_2O_3(a-Al_2O_3) can deform without fracturing up to 100% engineering strain when prepared as thin film samples with thicknesses below 100 nm [4], and later that the plasticity extends to microscale and to high experimental strain rates [5]. As the request for more durable materials ever increases, a deeper understanding of the structural basis of mechanical properties of a-Al_2O_3 is highly important.

For an amorphous material, observing a glass transition during the heating or quenching process categorizes it as a glass [6,7]. Both of these material groups are widely valued for their exceptional functionality [8,9]. Glass materials can be synthesized through a melt-quench process, which is expected to involve a glass transition. For good glass formers, such as SiO_2 and B_2O_3 [10], glass transition can occur at a relatively low cooling rate. However, nearly any material can be prepared in an amorphous state by sufficiently increasing the cooling rate [11,12].

From the perspective of Zachariasen's rules [13], Al_2O_3 does not qualify as a good glass former from a thermodynamic standpoint. Notably, amorphous alumina can be synthesized mainly using gas-phase methods such as physical and chemical vapor deposition and by chemical synthesis [5,14]. Nonetheless, there is no evidence that Al_2O_3 could exhibit a glass transition. Taking into account the extreme quench rate needed to produce amorphous Al_2O_3, the other possibility is that measuring the glass transition temperature using current experimental techniques is simply very difficult. Consequently, investigations into the glass transition of alumina are infrequent, but hold substantial importance. To our knowledge, only one documented measurement of the glass transition temperature (T_g) exists in the literature [14], along with a limited number of computational studies [15].

* Corresponding author.
E-mail address: jiahui.zhang@helsinki.fi (J. Zhang).
[1] These authors contributed equally to this work.

https://doi.org/10.1016/j.jnoncrysol.2024.122840
Received 27 November 2023; Received in revised form 16 January 2024; Accepted 17 January 2024
Available online 23 January 2024

The determination of the glass transition temperature for amorphous alumina is fundamental to advancing our understanding of this material and the whole concept of glass transition.

There are multiple definitions of the glass transition temperature. For example, the following lists different ways used to define T_g:

1. The temperature at which the shear viscosity reaches 1×10^{13} poise when cooling down the liquid;
2. The drastic change in specific heat capacity (ΔC_p) when heating the material.
3. The intersection of the liquid and amorphous portions of the potential energy versus temperature curve (in atomistic simulations).

The cooling rate affects the glass transition temperature when creating glasses. A higher cooling rate leaves less relaxation time for the atoms to sample their energy minimum, resulting in higher T_g [12,16]. Therefore, different T_g indicates that atoms are 'frozen' into different structures. The obtained structure can significantly alter the material properties. For example, a computational study reported that if amorphous silica (a-SiO_2) is quenched at a high enough cooling rate, it could withstand 50% tensile strain without fracture [17]. In contrast, experimentally reproducible quench rates for a-SiO_2 always produce a brittle fracture under tension, without plasticity, excluding some known size related anomalies observed at extreme nanoscale [18], and anomalies occurring under the influence of an electron beam [19]. Even though experimentally synthesized Al_2O_3 can show exceptional ductility, as demonstrated in the literature, the influence of the cooling rate on the mechanical properties is unclear and requires a more detailed characterization. Experimental estimation of the cooling rate required to prepare amorphous alumina is around 1×10^{10} K/s [20]. In this case, computational methods can be helpful because such high cooling rates are easy to reach. Tools such as molecular dynamics (MD) simulation methods have been applied using relatively small a-Al_2O_3 structures in previous studies [14,21,22]. Although a small system size can help reduce the computing power cost, it is accompanied by limitations such as finite-size effects and lack of long-range order [17,23].

In this work, we first investigate the glass transition in Al_2O_3 and measure the glass transition temperature (T_g) of Al_2O_3 as a function of cooling rate q using the molecular dynamics method. The produced Al_2O_3 glass systems are characterized, and tensile test simulations are performed on obtained structures to investigate how the cooling rate affects the mechanical properties. Structural analysis is performed with multiple methods on both the quenched and strained structures to study the structural differences caused by different cooling rates.

2. Methodology

2.1. Interatomic potential of Al_2O_3

The interatomic force field of classical MD greatly impacts the results and should be chosen carefully. The partial-charge Buckingham form potential parameters of Matsui [24] are adopted to describe alumina structures. Although the potential model has a simple form, it has shown the ability to reproduce experimental results in both the crystalline and liquid phases of alumina [25–29]. Our previous work verified that the potential could also provide comparable results with experiments regarding the plastic behavior of amorphous alumina [4,5]. The chosen potential is formulated as

$$U_{ij}(r_{ij}) = \frac{Z_i Z_j}{4\pi\epsilon_0}\frac{1}{r_{ij}} + Ae^{-r_{ij}/\rho} - \frac{C}{r_{ij}^6}, \tag{1}$$

where U_{ij} is the pair potential of atom i and j, Z_i and Z_j are the effective charges of the atoms, ϵ_0 is the vacuum permeability, r_{ij} is the distance between the atoms i and j. Constants A, ρ are potential repulsion parameters, and C is the Van der Waals constant. Table 1 shows the potential parameters.

All simulations were performed using the LAMMPS code [30].

Table 1
Potential parameters of Coulomb–Buckingham potential for a-Al_2O_3 obtained using the parameter values and combination rules from Matsui [24].

	A (eV)	ρ (Å)	C (eV·Å^6)
Al–Al	31571310.74	0.068	14.05114560
Al–O	28477.25737	0.172	34.57833522
O–O	6462.75033	0.276	85.09350771

	Mass (u)	Charge (C)
Al	26.9815	1.4175
O	15.9994	−0.9450

2.2. Preparation of alumina

The simulated alumina is prepared through a melt-quenching process from an initial crystalline structure. The initial system of 115,200 atoms is created by multiplying the unit cell until the desired monoclinic shape and size gives us a 110 × 90 × 110 Å^3 structure. The system is heated from 300 K to 4000 K in a constant-temperature-and-pressure ensemble (NPT) in zero pressure for 1 ns with a timestep of Δt = 0.5 fs. The Nose–Hoover algorithm is used in controlling the temperature and pressure. The system is then equilibrated at 4000 K for 250 ps with the same Δt. Periodic boundary conditions (PBC) are applied in all dimensions, which means there are no surfaces in the structure. This yielded a heating rate of 3.7×10^{12} K/s.

The melt is quenched from 4000 K to 50 K with cooling rates (q) from 1×10^{10} K/s to 5×10^{13} K/s. The quenching simulations are performed with the time step of Δt = 1 fs in NPT ensemble using periodic boundary conditions. The number of steps is changed accordingly to achieve the desired q. For $q = 1\times10^{10}$ K/s the quenching includes two parts. At the first stage, the melt is quenched from 4000 K to 2000 K with $q = 1 \times 10^{12}$ K/s in 1 ns to shorten the computation time. After confirming that the structure is still a melt, it is quenched to 50 K at 1×10^{10} K/s. This specific simulation has a total time length of ~200 million steps. Because this particular structure crystallized and was consequently not quantitatively characterized, the fact that this quenching simulation is divided into two stages does not bring new variables to the following discussions.

Moreover, a separate quenching is performed in such a way that energy minimization is performed on the 4000 K melt directly using the conjugate-gradient algorithm. The obtained structure is regarded as quenched with a cooling rate approaching infinity in later analysis.

2.3. Tensile test simulations

The tensile test simulations are performed by first equilibrating the quenched systems at 50 K for 1 ns with Δt = 0.5 fs. The systems are then heated to 300 K with a heating rate of 1×10^{12} K/s for 250 ps, to measure the mechanical properties near room temperature.

Tensile deformation is performed by adjusting the simulation box size every timestep. To avoid artificial ductility, we used a constant engineering strain rate of 1×10^9 s^{-1}, which has been proved in our previous investigation to be able to produce comparable stress–strain curves with experiments [5]. We also checked that the simulation box is large enough to meet the criteria proposed by Yuan et al. [17] so that size effects are controlled at a reasonable level. The structure is then equilibrated for 1,600,000 steps. NPT ensemble with zero pressure is applied in the other two directions, and the temperature is kept at 300 K. The Nose–Hoover algorithm is used similarly with the quenching process. Stress in this study specifically refers to true stress. Engineering strain is used in later analysis and discussions, which is defined as

$$\varepsilon = \frac{L - L_0}{L_0}, \tag{2}$$

where L_0 is the unstrained length of the system on the deformed dimension and L is the length at investigated strain.

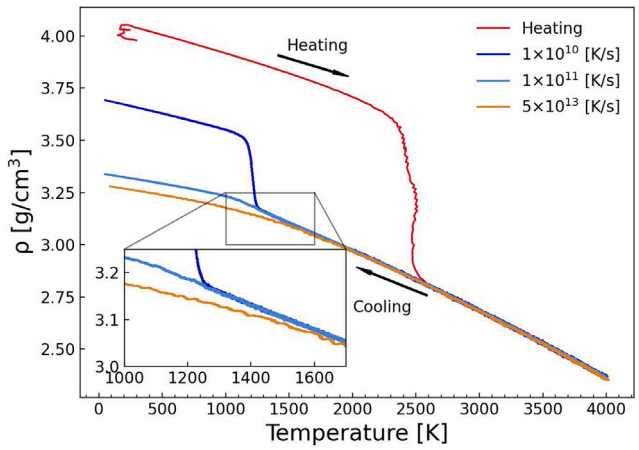

Fig. 1. Heating and quenching processes of Al_2O_3. Density as a function of temperature is compared for the 1×10^{11} and 5×10^{13} K/s cooling rates. For quenching with a cooling rate of 1×10^{10} K/s, the system transitions to nanocrystalline structure at around 1250 K.

2.4. Structural analysis

The radial distribution functions (RDF) and partial radial distribution functions (PRDF) are computed using OVITO software [31]. The bond angle distributions (BAD) are computed for systems quenched to 50 K also using OVITO. The pairwise cutoff distances used in the calculation of BADs are the following: $r_{Al-Al} = 3.8$ Å, $r_{Al-O} = 2.3$ Å and $r_{O-O} = 3.4$ Å, and are obtained as the positions of the first minimum in PRDFs.

Ring statistics for the structures are calculated with the algorithm of Yuan and Cormack [32], which gives the statistics of the primitive rings. The statistics are calculated from an Al atom and hops are counted from Al to Al atom via a bonded oxygen atom. The cutoff radius of 2.3 Å for the Al–O bond is used for all cases.

The coordination number analysis uses a cutoff distance of r_c = 2.3 Å. To perform polyhedral analysis, a center Al atom and its bonded O atoms are treated as a whole and regarded as the basic unit, namely a polyhedron. By counting the maximum number of O atoms that one polyhedron is sharing with any of its neighboring polyhedra, they are categorized as corner-sharing (one shared O atom), edge-sharing (two shared O atoms), and face-sharing polyhedron (three shared O atoms).

3. Results

3.1. Glass transition temperature

First, we determined the melting temperature of alumina by heating the system to 4000 K and analyzing the density change with respect to temperature. In Fig. 1, it is evident that the melting event occurs at ~2500 K, with a corresponding density change of approximately 20%. This observation aligns well with the reported experimental volume change during freezing as documented in Ref. [33]. It is worth noting that our simulated melting temperature slightly exceeds the reported experimental value of 2330 K, as documented in Refs. [34,35]. This discrepancy is common in molecular dynamics (MD) simulations, as experimental samples inevitably possess free surfaces and processing defects that facilitate liquid formation and lower the melting temperatures. It is also known that high heating rates lead to "hysteresis" of the melting point of crystals [36].

The molten Al_2O_3 is subsequently quenched using various cooling rates. Here we pick results for $q = 1\times10^{10}$ K/s, 1×10^{11} K/s, and 5×10^{13} K/s, respectively, as illustrated in Fig. 1. During the quenching process, the material undergoes densification as the kinetic energy of the atoms decreases. The glass transition is here potentially indicated by a change in the slope. A higher q value results in a shorter time for atoms to rearrange themselves into the energetically most favorable configuration, leading to structural property alterations, as evidenced by the final density shown here. Notably, at the lowest quenching rate of $q = 1\times10^{10}$ K/s, the system undergoes crystallization at approximately 1250 K instead of a glass transition. This results in the formation of a nanocrystalline structure, as shown in Fig. S2. Consequently, it is advisable to avoid q equal or lower than 1×10^{10} K/s when aiming to prepare amorphous Al_2O_3 in atomistic simulations.

Table 2
Glass transition temperature T_g of alumina systems estimated from different cooling rates using the potential energy ($T_g^{E_p}$) data.

q /K·s^{-1}	$T_g^{E_p}$ /K
1×10^{11}	921.6
2×10^{11}	943.0
5×10^{11}	968.3
1×10^{12}	983.1
2×10^{12}	1009.5
5×10^{12}	1043.6
1×10^{13}	1070.6
2×10^{13}	1103.8
5×10^{13}	1138.2

To quantitatively determine the glass transition temperature T_g, we conduct a fitting analysis on the potential energy (E_p) of the systems as a function of temperature, as shown in Fig. 2(a). The T_g is identified as a change in the slope of potential energy and determined as the intersection point of two fitted lines, which are drawn in Fig. 2(a). Ranging from $q = 1\times10^{11}$ to 5×10^{13} K/s, the T_g increases from 922 to 1138 K, respectively, as listed in Table 2.

We fit the T_g results with a functional form of the Vogel–Fulcher relation [16]:

$$T_g = T_0 - \frac{A}{\ln(B\cdot q)}, \tag{3}$$

where A and B are constants, and T_0 is the asymptotic value of T_g when using infinitesimal cooling and heating rates. In Fig. 2(b), we show the original data and fitted relation between T_g and cooling rates (q). Using the T_g values obtained from Fig. 2(b), we determined $A = 1.332\times10^4$ K, $B = 1.240\times10^{-21}$ s/K, and $T_0 = 338.4$ K. In our case, the T_0 we obtained is notably lower than the experimental result of 743 K [14]. Different from our method, this experimental value of T_g is obtained through heating the structure prepared using electrochemical anodization. The discrepancy between T_0 and experimental measured T_g is evident. Possible explanations involve the intrinsic ultra-high cooling rate needed to prepare amorphous alumina and the equivalence between T_0 and T_g for some materials. This discrepancy will be addressed in detail in the Discussion part. Additionally, T_g is not estimated for the data associated with the infinite cooling rate since actual cooling is not performed for that particular sample.

3.2. Tensile test

At a fixed temperature of 300 K, ten systems that underwent quenching at different cooling rates were subjected to tensile deformation at a fixed strain rate of 1×10^9 s^{-1}. The resulting stress–strain curves are presented in Fig. 3(a), with maximum stress at corresponding strain (σ_{max}, ε_{max}) shown by diamond markers. Results show evident room-temperature plasticity in all simulated structures. For the case of an infinite cooling rate, we define the stress at 10% strain as the maximum stress in subsequent discussions. As the cooling rate increased from $q = 1\times10^{11}$ K/s to 5×10^{13} K/s, a notable decrease in maximum stress occurs, from 7.8 GPa to 5.7 GPa. Interestingly, the structure quenched with an infinite cooling rate exhibits no discernible hump in the stress data. Instead, the σ_{max} is approximately 4.1 GPa and the stress remains nearly constant throughout the stretching. However,

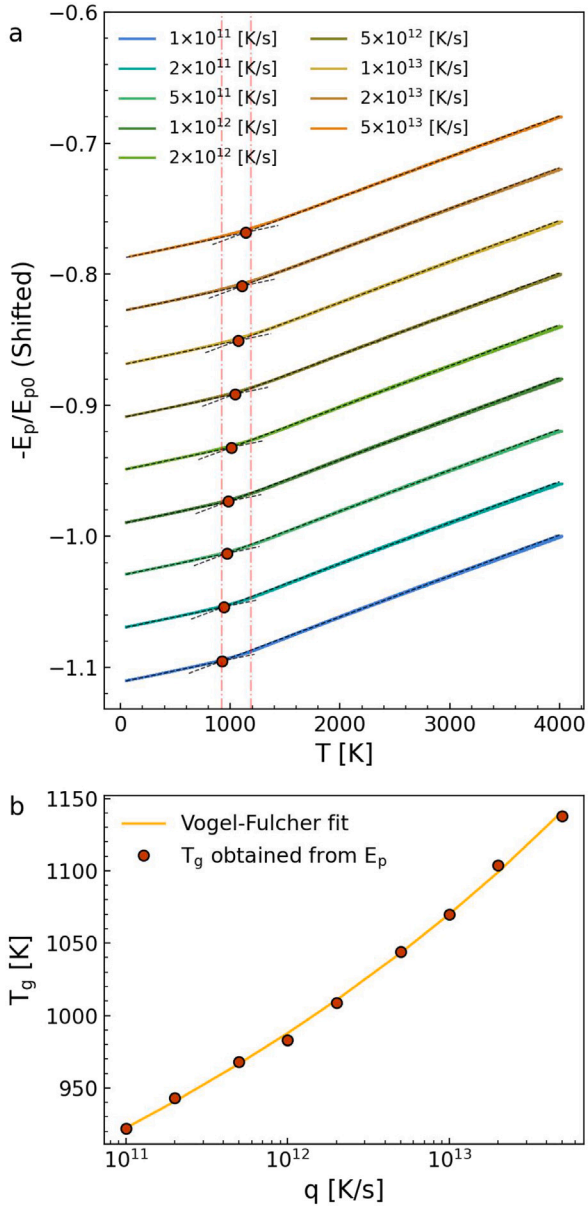

Fig. 2. (a) Potential energy of alumina systems as a function of temperature during quenching. Energy is scaled by the potential energy of the 4000 K liquid(E_{p0}). Curves with different cooling rates are shifted in the y-axis for clarity. Glass transition temperatures T_g are calculated as the intersections of the separate linear fits of the potential energy curves (gray dashed lines) and are marked with red circles. Vertical red lines help locate the range of T_g values determined here. (b) The glass transition temperature is determined from the potential energy as a function of cooling rates and fit of the data to Eq. (3).

despite the systematic reduction in σ_{max} with higher cooling rates, the stresses converge to nearly identical values (4.4 GPa) at 50% strain for all structures. We denote the stress and strain at 50% strain as σ_{flow} and ϵ_{flow}, respectively. In Fig. 3(b), we present σ_{max} and σ_{flow} as functions of q. It is evident that with an increasing cooling rate, σ_{max} experiences a significant decrease. Remarkably, at an infinite cooling rate, the difference between σ_{max} and σ_{flow} is nearly negligible. As stress in amorphous materials is closely related to the prevailing atomic structure, the results indicate that the liquid-like structure cooled at an infinite cooling rate has the least amount of atomic friction, a property comparable to lattice friction (Peierls barrier) in crystals, and the structures cooled at lower rates tend to converge towards an identical structure, as the atoms gain mobility during plastic deformation.

3.3. Structural analysis

Varied mechanical behaviors indicate possible structural differences formed during glass transition. Further quantitative characterizations are needed to investigate the structural differences. The densities and atomic densities of the equilibrated systems in 50 K are shown in Fig. 4 where a linear behavior in a semi-logarithmic plot can be observed. These two values decrease by 1.8% when increasing the q from 1×10^{11} K/s to 5×10^{13} K/s. Experimental measurements of the density range from 3.05 to 3.10 g/cm^3 [14,37], but they do not correspond to any cooling rate. Next, we characterized the structures using different structural parameters.

The comparison of radial distribution function (RDF), partial radial distribution function (PRDF), and bond angle distribution (BAD) results among different structures are shown in Figs. 5(a–g). There are no discernible differences in the short-range order (SRO) of the system structures, even as the cooling rate (q) varies over three orders of magnitude. All systems exhibit an identical full width at half maximum (FWHM) of 1.75 ± 0.09 Å for the first peak (Al–O) in the RDF. The FWHM values for the first Al–Al peak and O–O peak are 3.08 ± 0.54 Å and 2.74 ± 0.40 Å respectively. These values closely align with the experimental results of Refs. [14,37] and computational results reported in Refs. [21,38]. For the system quenched with an infinitely fast cooling rate, the position of the PRDF peaks still match other structures, only the distributions are broader than normally quenched samples. Bond angle distributions could also reflect the coordination distribution of atoms. As depicted in Figs. 5(d–g), BAD results exhibit minor discrepancies in the peak positions, indicating they have highly similar coordination distributions.

Next, we employed ring statistics analysis to characterize the medium-range order of the amorphous materials in our study, as presented in Fig. 6. We included computational data from Hashimoto et al. [14] for comparison. As the cooling rate increases from 1×10^{11} K/s to 1×10^{13} K/s, a noteworthy transformation is observed in the distribution peak, shifting from $N = 4$ to $N = 5$, except for the structure subjected to an infinitely fast cooling rate. To quantitatively assess these changes for the as-quenched structures at ϵ=0(=ϵ_{init}), we have calculated the averages ($\langle n_{ring} \rangle$) and standard deviations (σ_{ring}) of the ring statistics, which are presented in Figs. 6(b) and (c) under the legend 'initial.' The average experiences a 5.5% increase, while the standard deviation exhibits a 23.8% increase as q increases from 1×10^{11} K/s to infinity. Notably, the similar value of flow stress σ_{flow} at 50% strain suggests that the systems may converge towards a similar atomic structure at high strain. Results from offloading simulations (see Fig. S3) support this hypothesis, indicating that when the stress is released, all structures return to the same strain value and exhibit a strikingly similar unloading behavior, while the initial loading behavior is distinctly different. To further investigate whether the differently quenched materials all converge to a similar atomic structure during plastic flow, we include the structures at strain points ϵ_{max} and ϵ_{flow} in our ring analysis in 6(b–c), to explore the influence of mechanical work on the structure indicated by 'maximum' and 'flow' in the figure, respectively. Results show that the $\langle n_{ring} \rangle$ of structures show a highly similar trend from 'initial' to 'maximum' stress, but when the system reaches a steady state flow stress at ϵ_{flow}, the differences between $\langle n_{ring} \rangle$ become negligible among all structures including the system quenched at an infinite rate. This further supports the hypothesis that plasticity allows the material to dissipate stored elastic strain energy and converge towards an identical structure despite the specific thermal history that initially forms a unique amorphous structure upon quenching.

We then employ two distinct analytical methods to probe the structural information: coordination analysis, which unveils short-range order information by examining the interactions between Al and O atoms, and polyhedral analysis, which delves into longer-distance atom configurations. In our comprehensive analysis, we assess the structure

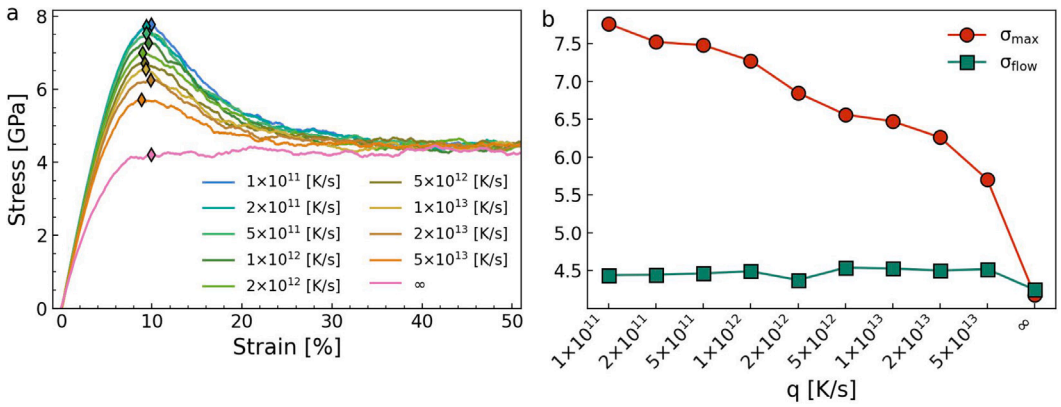

Fig. 3. (a) Stress–strain curve of systems quenched with different cooling rates. Tensile tests are performed at 300 K. The maximum stresses and strains (σ_{max}, ϵ_{max}) are marked with diamond markers. (b) σ_{max} (maximum stress) and σ_{flow} (stress at 50% strain) of systems as functions of q.

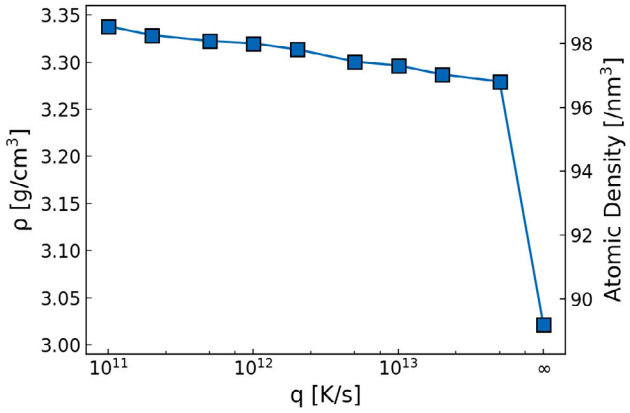

Fig. 4. Densities of the quenched systems at 50 K as a function of cooling rates. The x-axis is set to logarithmic to show the correlation between densities and cooling rates.

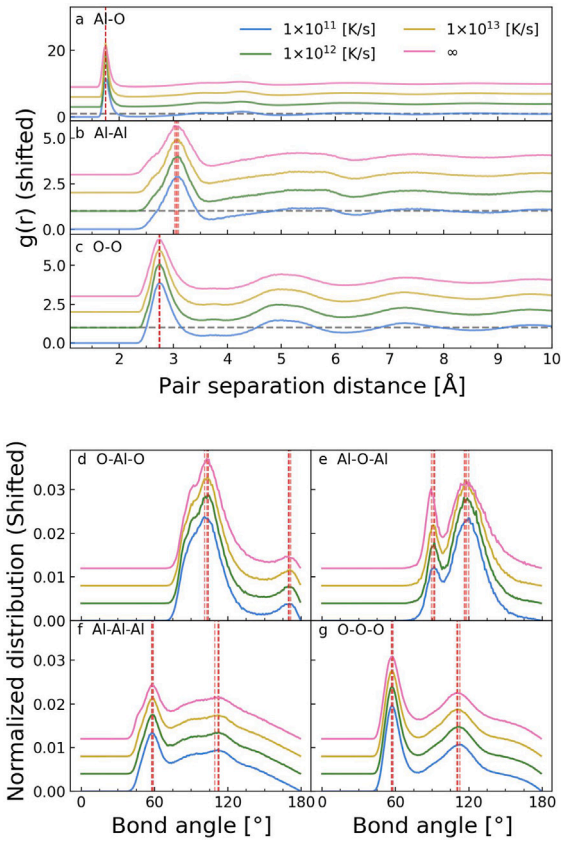

Fig. 5. (a–c) PRDFs of (a) Al–O (b) Al–Al and (c) O–O atoms for structures quenched with different cooling rates. Gray horizontal dashed lines represent $g(r) = 1$ which describes the absence of medium-range order (MRO). Results are shifted for clarity. (d–g) Normalized bond angle distribution of (d) O–Al–O angles (e) Al–O–Al angles (f) Al–Al–Al angles and (g) O–O–O angles. The cutoff distances for Al–Al, Al–O and O–O of 3.8, 2.3 and 3.4 Å, respectively, are used. Results are shifted for clarity. Peaks of each PRDF and BAD curve are marked with a vertical dashed red line.

at three key strain points in each tensile simulation: ϵ_{init}, ϵ_{max}, and ϵ_{flow}. These three critical stages on the stress–strain curves for each analysis set are represented as markers in Fig. 7. Figs. 7(a–f) illustrate the coordination changes of Al and O atoms with respect to q. Notation Al_n stands for an aluminum ion surrounded by n oxygen ions as nearest neighbors; similarly for O_n. In general, for a certain atom/polyhedron type, results show less variance between strain points as the cooling rate increases. This indicates that the initial structure prepared at a higher cooling rate has a lower energy barrier to overcome when reaching the flow structure, i.e., the structure at flow stress. However, though higher cooling rates yield structures that are closer to liquid structure, the flow structure is still quite different from the liquid. To clarify this fact and avoid introducing a new variable to this study, comparison of the structural information has been compared and supplemented as Fig. S6. Although it is suspected that the infinite cooling rate structure or the flow structure might be very close to the structure in the liquid phase, results show that the latter is distinct and close to none of the former two structures. Thus, we can draw a preliminary conclusion that the flow structure is more like a non-equilibrium structure.

To compare how sensitive the methods we used in characterizing the subtle difference between structures, in Table 3, we calculated the absolute fraction difference for each atom/polyhedron type between the fastest and slowest cooling rates. In our case, these values are also the maximum differences of their corresponding data set. Since the structures converge to an almost identical final flow structure, the largest structural difference between all cooling rates can only be found in the initial structures. Among the initial structures, the general trends are that as the cooling rate increases, the fractions of Al_4 and O_2 atoms rise. Contrarily, other atom types, including O_3, O_4, Al_5, and Al_6 all decrease in fraction. The absolute maximum fraction difference for Al and O atoms is 6.80% and 5.87%, respectively. But we can see that compared to polyhedral analysis, the sudden change between the infinite cooling rate and others contributes greatly to the maximum fraction difference. It is worth remarking that the high fraction of O_3 atoms is a clear proof that alumina as a glass former violates Zachariasen's rules [13]. The experimental results in the literature verify the high

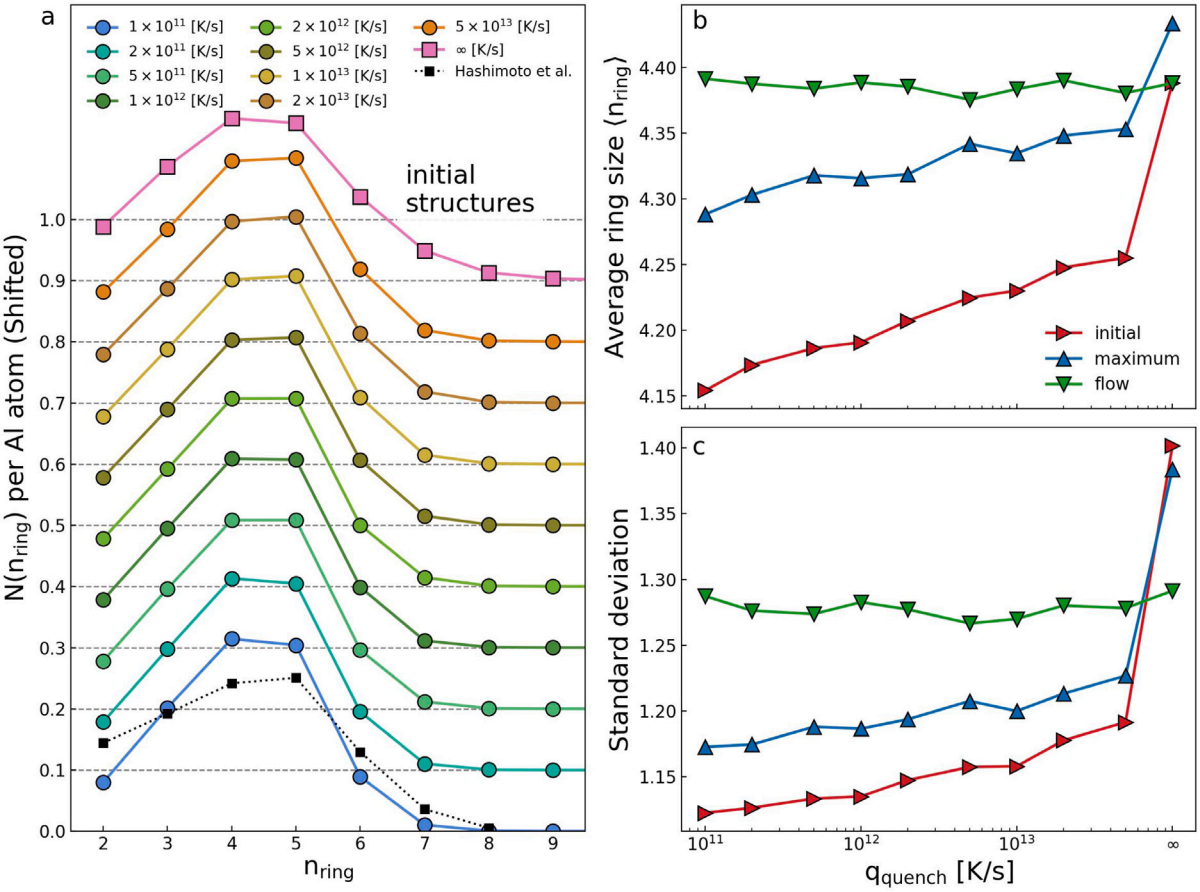

Fig. 6. Ring statistics of a-Al_2O_3 structures quenched at different q. (a) Ring size distributions for different cooling rates. The dashed black line results from Hashimoto et al. [14]. Results are shifted for clarity, and the horizontal dashed gray line is the baseline for each data set. (b) The average ring size for different cooling rates. Curves labeled 'initial', 'maximum' and 'flow' denote the data at ϵ_{init}, ϵ_{max} and ϵ_{flow}, respectively. (See Fig. 3) (c) Standard deviation of the ring size distributions for different cooling rates.

fraction of over-coordinated oxygen atoms compared to conventional oxide glasses [14,39,40], indicating that a modification of the principles is possibly needed. For polyhedral analysis, Hashimoto et al. [14] reported that in glass Al_2O_3, 79.4% of polyhedral connections are corner-sharing, while 19.3% are edge-sharing. In contrast, Figs. 7(g–i) demonstrates that our simulations yield a more balanced distribution of corner and edge-sharing connections in glass Al_2O_3. This variation can be attributed to the fact that Hashimoto et al. prepared the amorphous samples through electrochemical anodization, in contrast to melting quenching simulated in this study, and they obtained the atomic-level structures using reverse Monte Carlo simulations, fitting them to X-ray diffraction and neutron scattering data. Notably, the data in Fig. 7 shows that as q increases, corner-sharing connections transition to edge-sharing connections, with a negligible 0.25% change observed in face-sharing connections, which were initially low in number.

Additionally, polyhedral analysis paints a clearer picture of the structures throughout the tensile test. Figs. 7(g–i) shows a higher fraction of corner-sharing polyhedra at the maximum strain point, consistent with the stress humps in stress–strain results. Meanwhile, the fraction of edge-sharing polyhedra decreases accordingly. It has been computationally investigated before that in densified amorphous silica the fraction of edge-sharing polyhedra would decrease as tensile strain increases, and partly recover when approaching flow stress [41]. This is probably because from elastic loading up to yield stress, the elastic energy is stored by breaking bonds in edge-sharing polyhedra. The temporary conversion from edge-sharing polyhedra to corner-sharing polyhedra results in an increase at ϵ_{max} in 7(g–i).

Notably, there is no discernible hump in the stress–strain curve for the structure quenched at an infinitely fast cooling rate, and no increase

Table 3
Maximum difference of Al_n, O_n and polyhedron type at different strain points between all structures based on the data shown in Fig. 7.

	@ ϵ_{init}	@ ϵ_{max}	@ ϵ_{flow}
Al_4	6.80	3.23	0.28
Al_5	2.85	1.95	0.20
Al_6	4.08	1.35	0.13
O_2	5.87	2.73	0.30
O_3	4.28	2.25	0.33
O_4	1.53	0.47	0.05
Corner-sharing	7.35	7.00	0.10
Edge-sharing	7.61	6.77	0.09
Face-sharing	0.25	0.23	0.01

in the fraction of corner-sharing polyhedra is observed. From the above-mentioned showcases, we can conclude that atomistic analysis alone is not adequate to characterize plasticity related mechanisms. Upon comparing these characterization methods, it is evident that polyhedral analysis yields differences more substantial at ϵ_{init} and ϵ_{max} compared to atomic-level characterization. Since polyhedral analysis characterizes amorphous structures at larger scales than atomic-level analysis, we can say that we are detecting distinctions in the medium-range order.

4. Discussion

As cooling rates span two and a half orders of magnitude, we observe a significant 217 K change in T_g, as determined from potential energy results. To put this in perspective, it is worth noting that, in a reference simulation study, a change of 350 K in T_g has been

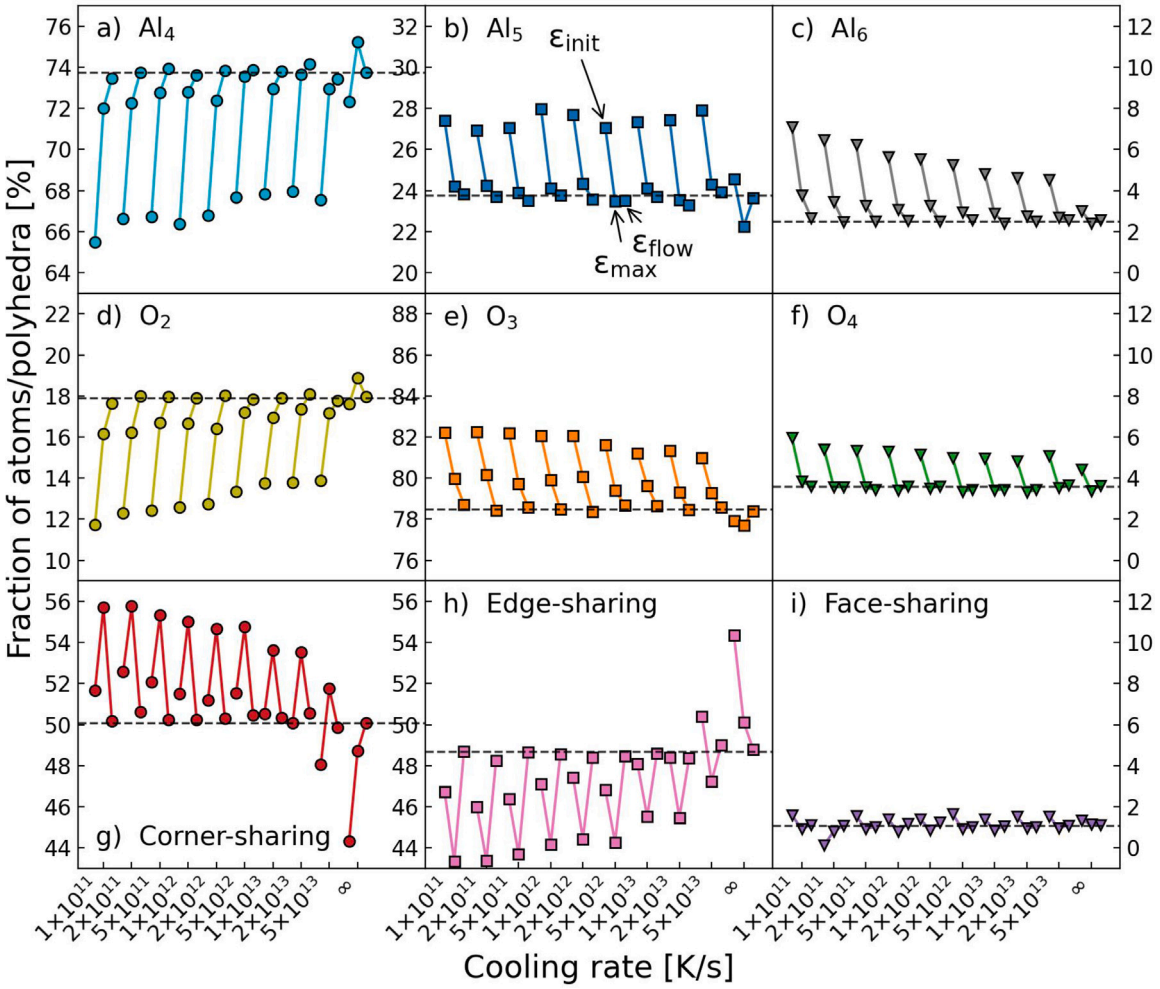

Fig. 7. Coordination analysis results of (a–c) Al (d–f) O atoms, and (g–i) polyhedron type analysis for all systems. For each atom or polyhedron type, the markers from left to right denote the corresponding results at ϵ_{init}, ϵ_{max}, and ϵ_{flow}. The x-axis is the cooling rate used in creating the structure, the unit is K/s, and the y-axis is the atomic or polyhedral fraction. The dashed line in each subfigure shows the convergence of the results at flow stress. The same y-axis length is used for comparison reasons.

reported for amorphous silica when the cooling rate varies by 1.5 orders of magnitude [16]. It is apparent that the methods commonly used in experiments to estimate T_g are no longer convenient within the computational time scales, particularly at cooling rates exceeding 1×10^{10} K/s. Experimental techniques often rely on tracking the specific heat capacity (ΔC_p) as a function of temperature during heating or cooling to determine T_g [42,43]. Using supplementary heating simulations, we verified that a consistent trend can be observed between the T_g and the cooling rate (S4). However, in the simulation, a new variant will emerge, which is the initial structure used in heating. It differs from the initial structure used in quenching, which is the same melt for all cooling rates. Additionally, at high cooling rates typical for simulations, the glass transition region becomes wider on the $\Delta C_p - T$ plot, making the determination of T_g more challenging. Furthermore, calculating ΔC_p as the second derivative of potential energy, especially when quenching is performed at zero pressure, often results in unacceptable noise in the data. It is essential to recognize that the glass transition is not a sudden, abrupt phase transition, and the term 'glass transition region' is often more appropriate to describe its nature [12]. In summary, for atomistic simulations, estimating T_g based on the change in potential energy during cooling is more suitable than relying on the change in heat capacity.

Although the VF equation is believed only behave well in describing the viscosity–temperature correlation of glass formers at high temperature and low viscosity conditions, we attempt to construct a semi-empirical model with this equation, in order to provide a practical way to extrapolate T_g from limited data. The VF equation has been previously used to describe the T_g-q correlation in silica [16], but it has never been used for alumina. Angell et al. [44] proposed that the VF equation provides an adequate description of the dependence of glass transition temperature on cooling rate for 'strong' glass formers but performs inadequately for 'fragile' glass formers. Although future research is still needed to definitively determine whether alumina is a 'strong' or 'fragile' glass former, its stringent cooling rate requirement for achieving glass transition suggests that it is unlikely to be a 'strong' glass former. Our fitting results suggest that the Vogel–Fulcher equation does indeed provide a good fit within the studied cooling rate range. However, several possible explanations for this apparent exception exist. Firstly, it is important to note that our results cover less than three orders of magnitude, which might be insufficient to evaluate the Vogel–Fulcher equation's performance conclusively. Secondly, the pre-exponent constant B is seven orders of magnitude lower than the typical value range considered physically meaningful, even though the fitting results are satisfactory. Therefore, we cannot yet conclusively assert that the Vogel–Fulcher equation accurately describes the dependence of glass transition temperature on the cooling rate in amorphous alumina. Importantly, in the case of materials like a-SiO_2, T_0 is comparable to the experimental T_g because laboratory cooling rates can be slow enough to be regarded as effectively infinitesimal. However, this does not hold true for a-Al_2O_3, which, if synthesized by melt quenching, can only be prepared with sufficiently high cooling rates, as confirmed by both experimental estimations in literature [4]

and computational results in our study. Consequently, T_g obtained from experiments can no longer be considered as achieved under infinitesimal cooling rates. This difference accounts for the notable deviation between experimental T_g and T_0 observed in our investigation.

In our efforts to characterize the results using multiple analysis methods, it becomes evident that techniques primarily focusing on short-range order (SRO) alone are less effective compared to those capable of capturing medium-range order (MRO). Both coordination change and polyhedral analysis are adept at revealing structural distinctions among the quenched structures. However, they manifest these distinctions differently. The key divergence between coordination and polyhedral analyses lies in the fact that polyhedral analysis considers not only the nearest neighboring atoms but also those at second nearest neighbor distances or further. Similarly, ring statistics results underscore the importance of probing beyond nearest neighbors by showing significant variation in the average ring size among the initial structures. Although the precise significance of ring statistics in terms of the structure remains uncertain, it provides insights extending beyond the nearest neighbors similar to polyhedral analysis. Furthermore, in Fig. 7, we note that the fractions of polyhedral coordination exhibit a distinctive peak at maximum stress, indicating a temporary transition from edge-sharing to corner-sharing polyhedra at high stress. We noticed in our previous study, that by such a mechanism, amorphous alumina could temporarily store the elastic strain energy, and dissipate the energy through polyhedron-level neighbor change activity [41]. This behavior is observed in all structures featuring a stress–strain curve hump, but atomic-level coordination analysis fails to capture this phenomenon. This observation highlights the heightened sensitivity of polyhedral analysis in revealing structural changes within amorphous materials and underscores the significance of characterizing MRO.

As elucidated by tensile test simulations, it becomes evident that higher q values lead to lower maximum stress (σ_{max}). It is widely acknowledged that a higher cooling rate leaves less relaxation time for atoms to explore their minimum energy positions before being 'frozen' into positions associated with higher potential energies than crystalline phases. Therefore, the glass transition temperature (T_g) is often conceived as the fictive temperature at which the melt undergoes this 'freezing' process. A lower T_g suggests that the resultant glass can be described to be 'colder' compared to a glass with a higher T_g. This means that when subjected to a tensile force, more mechanical energy is needed to pull the atoms out from their potential energy well. Our findings indicate that the continuous input of mechanical energy performs a role similar to the steady supply of thermal energy. 'Colder' structures require more energy input than 'warmer' structures to facilitate 'melting', or in other words, the formation of viscous flow. In conclusion, higher q values result in higher T_g, making it easier for them to initiate the viscous flow. Additionally, the temperature during the tensile test affects both maximum stress and flow stresses (as seen in Fig. S1). Higher temperatures correspond to increased thermal vibrations of atoms, necessitating less energy to overcome energy barriers and promote the formation of viscous flow.

Characterization results show that strained structures exhibit similar flow stress levels at 50% strain and share comparable structural properties if the temperature remains constant. In the realm of metallic glasses, mechanical work has been demonstrated as a way to modify their nano-scale structure [45]. Our study suggests that mechanical work can also influence the structure of oxide glass materials. Tensile test simulations illustrate that introducing mechanical work through a constant strain rate operates akin to increasing the temperature. This process provides the necessary energy for local atom rearrangements and facilitates viscous flow. As depicted in Fig. S1 and also previous research [46], the flow stresses attained by different structures can be influenced by temperature. In summary, our observations in amorphous alumina indicate that mechanical deformation can induce effects akin to annealing at elevated temperatures. Structures that initially differ before stretching no longer exhibit discernible structural distinctions once they reach the flow stress state. However, the fundamental connection between activating the structure through mechanical work and thermal energy remains unclear and warrants further investigation.

Additionally, our results can give insight into why the glass transition temperature of amorphous aluminum oxide will be difficult to measure using standard calorimetric methods. Gas phase synthesis, such as pulsed laser deposition of amorphous alumina, typically enforces an ultra-high quench rate [20]. As our simulation results indicate that increasing the quench rate subsequently increases the T_g, this could mean that eventually, the T_g will approach the crystallization temperature T_c of liquid alumina, and in calorimetric measurements, the peaks produced by both will begin to overlap greatly. Therefore, gaining more resolution between the reactions, for example, by using ultra-high-speed calorimetry could help to solve the conundrum.

5. Conclusions

Alumina, while not a conventional glass former, exhibits a remarkable transition to a glassy state in molecular dynamics simulations when subjected to sufficiently high quenching rates. Based on the potential energy change during quenching, our estimation of the glass transition temperature spans a range from 922 K to 1138 K, corresponding to an increase over 2.5 orders of magnitude in cooling rate.

Tensile tests on structures quenched at various cooling rates reveal distinct mechanical properties. As the cooling rate decreases, the maximum strength increases. This observation suggests that less mechanical work is required to initiate plastic flow in structures quenched at higher cooling rates, primarily because they result in less energetically favorable structural configurations within a shorter time frame.

We employed multiple analytical tools, including coordination analysis, polyhedral analysis, and ring statistics, to scrutinize the quenched structures. Significantly, polyhedral analysis and ring statistics exhibit more pronounced differences than the widely used coordination analysis. This underscores the importance of employing analysis methods capable of capturing information over longer interatomic distances to enhance our understanding of plasticity mechanisms in amorphous oxide materials.

However, it is intriguing to note that these differences in stress levels vanish at 50% strain, indicating that different systems ultimately converge to identical flow stresses. Our structural analysis results further illuminate that this convergence extends beyond stress and encompasses all investigated structural parameters. With sufficient deformation, the influence of the initial quenching rate on the system's history diminishes, and mechanical work exhibits similar effects to thermal energy, effectively promoting a form of structural 'healing' towards the liquid-like state.

CRediT authorship contribution statement

Jiahui Zhang: Writing – review & editing, Writing – original draft, Validation, Methodology, Investigation, Formal analysis, Conceptualization. **Mikael De Meulder:** Writing – original draft, Data curation, Conceptualization. **Erkka J. Frankberg:** Validation, Supervision, Project administration, Funding acquisition. **Antti Kuronen:** Supervision, Resources, Funding acquisition.

Declaration of competing interest

The authors declare that they have no conflicts of interest.

Data availability

Data will be made available on request.

Acknowledgments

We acknowledge funding from the Academy of Finland project numbers 315451, 315453, 326426, 338750 and 332347.

The computational resources granted by the CSC – IT Center for Science projects 2003839 (LAPLAS Glass Plasticity at Room Temperature) and hy3898, Finland, and by the Finnish Grid and Cloud Infrastructure project (FGCI; urn:nbn:fi:research-infras-2016072533) are gratefully acknowledged.

Appendix A. Supplementary data

Supplementary material related to this article can be found online at https://doi.org/10.1016/j.jnoncrysol.2024.122840.

References

[1] A.K. Varshneya, Fundamentals of Inorganic Glasses, Elsevier, 2013.

[2] L. Wondraczek, J.C. Mauro, J. Eckert, U. Kühn, J. Horbach, J. Deubener, T. Rouxel, Towards ultrastrong glasses, Adv. Mater. 23 (2011) 4578–4586, http://dx.doi.org/10.1002/adma.201102795, URL https://onlinelibrary.wiley.com/doi/10.1002/adma.201102795.

[3] Y. Shi, J. Luo, F. Yuan, L. Huang, Intrinsic ductility of glassy solids, J. Appl. Phys. 115 (2014) http://dx.doi.org/10.1063/1.4862959, URL https://pubs.aip.org/jap/article/115/4/043528/345242/Intrinsic-ductility-of-glassy-solids.

[4] E.J. Frankberg, J. Kalikka, F.G. Ferré, L. Joly-Pottuz, T. Salminen, J. Hintikka, M. Hokka, S. Koneti, T. Douillard, B. Le Saint, P. Kreiml, M.J. Cordill, T. Epicier, D. Stauffer, M. Vanazzi, L. Roiban, J. Akola, F.D. Fonzo, E. Levänen, K. Masenelli-Varlot, Highly ductile amorphous oxide at room temperature and high strain rate, Science 366 (6467) (2019) 864–869, http://dx.doi.org/10.1126/science.aav1254.

[5] E.J. Frankberg, A. Lambai, J. Zhang, J. Kalikka, S. Khakalo, B. Paladino, M. Cabrioli, N.G. Mathews, T. Salminen, M. Hokka, J. Akola, A. Kuronen, E. Levänen, F.D. Fonzo, G. Mohanty, Exceptional microscale plasticity in amorphous aluminum oxide at room temperature, Adv. Mater. (2023) http://dx.doi.org/10.1002/adma.202303142.

[6] P.K. Gupta, Non-crystalline solids: Glasses and amorphous solids, J. Non-Cryst. Solids 195 (1996) 158–164, http://dx.doi.org/10.1016/0022-3093(95)00502-1.

[7] E.D. Zanotto, J.C. Mauro, The glassy state of matter: Its definition and ultimate fate, J. Non-Cryst. Solids 471 (2017) 490–495, http://dx.doi.org/10.1016/j.jnoncrysol.2017.05.019, URL https://linkinghub.elsevier.com/retrieve/pii/S0022309317302685.

[8] Y. Idota, T. Kubota, A. Matsufuji, Y. Maekawa, T. Miyasaka, Tin-based amorphous oxide: A high-capacity lithium-ion-storage material, Science 276 (5317) (1997) 1395–1397, http://dx.doi.org/10.1126/science.276.5317.1395, URL https://www.science.org/doi/abs/10.1126/science.276.5317.1395.

[9] J.Y. Kim, S.H. Kim, H.H. Lee, K. Lee, W. Ma, X. Gong, A.J. Heeger, New architecture for high-efficiency polymer photovoltaic cells using solution-based titanium oxide as an optical spacer, Adv. Mater. 18 (5) (2006) 572–576, http://dx.doi.org/10.1002/adma.200501825.

[10] M. Eigen, Chapter 12 - Oxide glasses, in: K. Rao (Ed.), Structural Chemistry of Glasses, Elsevier Science Ltd, Oxford, 2002, pp. 463–511, http://dx.doi.org/10.1016/B978-008043958-7/50030-3, URL https://www.sciencedirect.com/science/article/pii/B9780080439587500303.

[11] C.A. Angell, Perspective on the glass transition, J. Phys. Chem. Solids 49 (1988) 863–871, http://dx.doi.org/10.1016/0022-3697(88)90002-9, URL https://linkinghub.elsevier.com/retrieve/pii/0022369788900029.

[12] P.G. Debenedetti, F.H. Stillinger, Supercooled liquids and the glass transition, Nature 410 (2001) 259, URL www.nature.com.

[13] W.H. Zachariasen, The atomic arrangement in glass, J. Am. Chem. Soc. 54 (1932) 3841–3851, http://dx.doi.org/10.1021/ja01349a006, URL https://pubs.acs.org/doi/abs/10.1021/ja01349a006.

[14] H. Hashimoto, Y. Onodera, S. Tahara, S. Kohara, K. Yazawa, H. Segawa, M. Murakami, K. Ohara, Structure of alumina glass, Sci. Rep. 12 (1) (2022) 516, http://dx.doi.org/10.1038/s41598-021-04455-6, URL https://doi.org/10.1038/s41598-021-04455-6.

[15] C.G. Levi, V. Jayaram, J.J. Valencia, R. Mehrabian, Phase selection in electrohydrodynamic atomization of alumina, J. Mater. Res. 3 (1988) 969–983, http://dx.doi.org/10.1557/JMR.1988.0969, URL http://link.springer.com/10.1557/JMR.1988.0969.

[16] K. Vollmayr, W. Kob, K. Binder, Cooling-rate effects in amorphous silica: A computer-simulation study, Phys. Rev. B 54 (1996) 15808–15827, http://dx.doi.org/10.1103/PhysRevB.54.15808.

[17] F. Yuan, L. Huang, Molecular dynamics simulation of amorphous silica under uniaxial tension: From bulk to nanowire, J. Non-Cryst. Solids 358 (2012) 3481–3487, http://dx.doi.org/10.1016/j.jnoncrysol.2012.05.045.

[18] J. Luo, J. Wang, E. Bitzek, J.Y. Huang, H. Zheng, L. Tong, Q. Yang, J. Li, S.X. Mao, Size-dependent brittle-to-ductile transition in silica glass nanofibers, Nano Lett. 16 (2016) 105–113, http://dx.doi.org/10.1021/acs.nanolett.5b03070, URL https://pubs.acs.org/doi/10.1021/acs.nanolett.5b03070.

[19] K. Zheng, C. Wang, Y.-Q. Cheng, Y. Yue, X. Han, Z. Zhang, Z. Shan, S.X. Mao, M. Ye, Y. Yin, E. Ma, Electron-beam-assisted superplastic shaping of nanoscale amorphous silica, Nature Commun. 1 (2010) 24, http://dx.doi.org/10.1038/ncomms1021, URL https://www.nature.com/articles/ncomms1021.

[20] F.G. Ferré, E. Bertarelli, A. Chiodoni, D. Carnelli, D. Gastaldi, P. Vena, M.G. Beghi, F.D. Fonzo, The mechanical properties of a nanocrystalline Al2O3/a-Al2O3 composite coating measured by nanoindentation and Brillouin spectroscopy, Acta Mater. 61 (2013) 2662–2670, http://dx.doi.org/10.1016/j.actamat.2013.01.050.

[21] G. Gutiérrez, B. Johansson, Molecular dynamics study of structural properties of amorphous (formula presented), Phys. Rev. B 65 (10) (2002) 1–9, http://dx.doi.org/10.1103/PhysRevB.65.104202.

[22] P. Vashishta, R.K. Kalia, A. Nakano, J.P. Rino, Interaction potentials for alumina and molecular dynamics simulations of amorphous and liquid alumina, J. Appl. Phys. 103 (8) (2008) http://dx.doi.org/10.1063/1.2901171.

[23] Z. Zhang, S. Ispas, W. Kob, The critical role of the interaction potential and simulation protocol for the structural and mechanical properties of sodosilicate glasses, J. Non-Cryst. Solids 532 (2020) http://dx.doi.org/10.1016/j.jnoncrysol.2020.119895.

[24] M. Matsui, A transferable interatomic potential model for crystals and melts in the system CaO-MgO-Al_2O_3-SiO_2, Mineral. Mag. 58 (1994) 571–572.

[25] M. Matsui, Molecular dynamics study of the structures and bulk moduli of crystals in the system CaO-MgO-Al2O3-SiO2, Phys. Chem. Miner. 23 (6) (1996) 345–353, http://dx.doi.org/10.1007/BF00199500.

[26] M. Matsui, Molecular dynamics simulation of structures, bulk moduli, and volume thermal expansivities of silicate liquids in the system CaO-MgO-Al2O3-SiO2, Geophys. Res. Lett. 23 (4) (1996) 395–398, http://dx.doi.org/10.1029/96GL00260.

[27] A.B. Belonoshko, Melting of corundum using conventional and two-phase molecular dynamic simulation method, Phys. Chem. Miner. 25 (1998) 138–141, http://dx.doi.org/10.1007/s002690050096.

[28] G. Gutiérrez, A.B. Belonoshko, R. Ahuja, B. Johansson, Structural properties of liquid Al2O3: A molecular dynamics study, Phys. Rev. E 61 (3) (2000) 2723–2729.

[29] R. Ahuja, A. Belonoshko, B. Johansson, Melting and liquid structure of aluminum oxide using a molecular-dynamics simulation, Phys. Rev. E 57 (2) (1998) 1673–1676, http://dx.doi.org/10.1103/PhysRevE.57.1673, URL https://link.aps.org/doi/10.1103/PhysRevE.57.1673.

[30] A.P. Thompson, H.M. Aktulga, R. Berger, D.S. Bolintineanu, W.M. Brown, P.S. Crozier, P.J. in 't Veld, A. Kohlmeyer, S.G. Moore, T.D. Nguyen, R. Shan, M.J. Stevens, J. Tranchida, C. Trott, S.J. Plimpton, LAMMPS - a flexible simulation tool for particle-based materials modeling at the atomic, meso, and continuum scales, Comput. Phys. Comm. 271 (2022) 108171, http://dx.doi.org/10.1016/j.cpc.2021.108171.

[31] A. Stukowski, Visualization and analysis of atomistic simulation data with OVITO-the Open Visualization Tool, Modelling Simul. Mater. Sci. Eng. 18 (1) (2010) http://dx.doi.org/10.1088/0965-0393/18/1/015012.

[32] X. Yuan, A.N. Cormack, Efficient algorithm for primitive ring statistics in topological networks, Comput. Mater. Sci. 24 (2002) 343–360, http://dx.doi.org/10.1016/S0927-0256(01)00256-7.

[33] P. Tyrolerova, W.-K. Lu, Volume change on freezing of ALO,, J. Am. Ceram. Soc. 52 (2) (1969) 77–79, http://dx.doi.org/10.1111/j.1151-2916.1969.tb13344.x, URL https://ceramics.onlinelibrary.wiley.com/doi/abs/10.1111/j.1151-2916.1969.tb13344.x.

[34] P. Patnaik, K. (Firm), Handbook of Inorganic Chemicals, in: McGraw-Hill Handbooks, McGraw-Hill, 2003, URL https://books.google.fi/books?id=XqjTTzkvTEC.

[35] R.F. Geller, P.J. Yavorsky, Melting point of alpha.alumina, J. Res. Natl. Bur. Stand. 34 (1945).

[36] K. Chattopadhyay, R. Goswami, Melting and superheating of metals and alloys, Prog. Mater. Sci. 42 (1) (1997) 287–300, http://dx.doi.org/10.1016/S0079-6425(97)00030-3, URL https://www.sciencedirect.com/science/article/pii/S0079642597000303.

[37] C. Shi, O.L.G. Alderman, D. Berman, J. Du, J. Neuefeind, A. Tamalonis, J.K.R. Weber, J. You, C.J. Benmore, The structure of amorphous and deeply supercooled liquid alumina, Front. Mater. 6 (2019) http://dx.doi.org/10.3389/fmats.2019.00038, URL https://www.frontiersin.org/article/10.3389/fmats.2019.00038/full.

[38] T. Du, H. Liu, L. Tang, S.S. Sørensen, M. Bauchy, M.M. Smedskjaer, Predicting fracture propensity in amorphous alumina from its static structure using machine learning, ACS Nano 15 (2021) 17705–17716, http://dx.doi.org/10.1021/acsnano.1c05619, URL https://pubs.acs.org/doi/10.1021/acsnano.1c05619.

[39] S.K. Lee, S.B. Lee, S.Y. Park, Y.S. Yi, C.W. Ahn, Structure of amorphous aluminum oxide, Phys. Rev. Lett. 103 (2009) http://dx.doi.org/10.1103/PhysRevLett.103.095501.

[40] J. He, D. Avnir, L. Zhang, Sol-gel derived alumina glass: Mechanistic study of its structural evolution, Acta Mater. 174 (2019) 418–426, http://dx.doi.org/10.1016/j.actamat.2019.05.062.

[41] J. Zhang, E.J. Frankberg, J. Kalikka, A. Kuronen, Room temperature plasticity in amorphous SiO2 and amorphous Al2O3: A computational and topological study, Acta Mater. 259 (2023) 119223, http://dx.doi.org/10.1016/j.actamat.2023.119223, URL https://linkinghub.elsevier.com/retrieve/pii/S1359645423005530.

[42] R. Brüning, K. Samwer, Glass transition on long time scales, Phys. Rev. B 46 (1992) 11318–11322, http://dx.doi.org/10.1103/PhysRevB.46.11318, URL https://link.aps.org/doi/10.1103/PhysRevB.46.11318.

[43] C.T. Moynihan, A.J. Easteal, J. Wilder, J. Tucker, Dependence of the glass transition temperature on heating and cooling rate, J. Phys. Chem. 78 (1974) 2673–2677, http://dx.doi.org/10.1021/j100619a008, URL https://pubs.acs.org/doi/abs/10.1021/j100619a008.

[44] C.A. Angell, K.L. Ngai, G.B. McKenna, P.F. McMillan, S.W. Martin, Relaxation in glassforming liquids and amorphous solids, J. Appl. Phys. 88 (2000) 3113–3157, http://dx.doi.org/10.1063/1.1286035.

[45] Z. Fan, Q. Li, C. Fan, H. Wang, X. Zhang, Strategies to tailor serrated flows in metallic glasses, J. Mater. Res. 34 (2019) 1595–1607, http://dx.doi.org/10.1557/jmr.2018.446.

[46] J.M.D. Lane, Cooling rate and stress relaxation in silica melts and glasses via microsecond molecular dynamics, Phys. Rev. E (3) 92 (2015) http://dx.doi.org/10.1103/PhysRevE.92.012320.